INTERACTION OF THE FRICTION STIR WELDING TOOL AND WORK-PIECE AS INFLUENCED BY PROCESS PARAMETERS

By

Aaron Matthew Davis

A Thesis
Submitted to the Faculty of
Mississippi State University
in Partial Fulfillment for Requirements
for the Degree of Master of Science
in Mechanical Engineering,
in the Department of Mechanical Engineering

Mississippi State University

May 2010

ProQuest LLC
789 East Eisenhower Parkway
P.O. Box 1346
Ann Arbor, MI 48106-1346

INTERACTION OF THE FRICTION STIR WELDING TOOL AND WORK-PIECE AS INFLUENCED BY PROCESS PARAMETERS

By

Aaron Matthew Davis

Approved:

Judith Schneider Associate Professor Mechanical Engineering (Major Professor)	A.C. Nunes, Jr. Materials and Processes Laboratory NASA Marshall Space Flight Center (Committee Member)
Preston McGill Materials and Processes Laboratory NASA Marshall Space Flight Center (Committee Member)	Qian (Jenny) Du Associate Professor Electrical and Computer Engineering (Committee Member)
David Marcum Endowed Professor Graduate Coordinator Mechanical Engineering	Sarah A. Rajala Professor and Dean Bagley College of Engineering

Name: Aaron Matthew Davis

Date of Degree: May 1, 2010

Institution: Mississippi State University

Major Field: Mechanical Engineering

Major Professor: Dr. Judith Schneider

Title of Study: INTERACTION OF THE FRICTION STIR WELDING TOOL AND WORK-PIECE AS INFLUENCED BY PROCESS PARAMETERS

Pages in Study: 43

Candidate for Degree of Master of Science

Friction Stir Welding (FSW) is a solid-state joining process that is of special interest in joining aluminum and other alloys that are traditionally difficult to fusion weld. The energy required for this joining process is transmitted to the work-pieces through a rotating FSW tool. Modeling attempts, aimed at perfecting the process, rely on assumptions of the contact conditions present between the work-pieces and the FSW tool. Various studies have attempted to define these contact conditions. Both theoretical and experimental studies indicate the contact conditions between the work-piece and weld tool are unknown and may vary during the FSW process. To provide insight into the contact conditions, the objective of this study is to characterize the FSW nugget in terms of swept volume as indicated by the cross-sectional area and symmetry of the FSW nugget over a range of processing conditions.

DEDICATION

I would like to dedicate this research to my family and friends for their patience and support.

ACKNOWLEDGEMENTS

I would like to extend my sincerest gratitude to everyone who assisted with this research. I would especially like to thank my major advisor, Dr. Judith Schneider, who provided support and guidance throughout this process. Appreciation is also extended to Arthur C. Nunes, Jr. and Preston McGill for their invaluable suggestions and assistance. Finally, I would like to thank the NASA-Marshall Space Flight Center Cooperative Agreement # NNM04AA14A, which provided the funding to make this research possible.

TABLE OF CONTENTS

PAGE

LIST OF TABLES

LIST OF FIGURES

FIGURE PAGE

CHAPTER I

INTRODUCTION

Patented by The Welding Institute (TWI) in 1991, Friction Stir Welding (FSW) is a solid-state joining process that shows promise for joining metals that are difficult to fusion weld [1]. To begin the FSW, a non-consumable, rotating FSW tool is plunged into the work-piece. The rotating tool is then moved along the weld seam to plastically join the two pieces of metal. Heat produced by the rotating FSW tool softens the work-piece and allows the FSW tool to plastically deform the metal in a stirring fashion. Figure 1 summarizes the terminology associated with the FSW process. On the advancing side (AS) of the FSW, the tool feed and the tool rotation directions coincide. The tool feed direction and tool rotation direction are opposite on the retreating side (RS) of the FSW. This results in an asymmetric flow field around the weld tool. A cross sectional view of the FSW is referred to as the transverse view while the top view is referred to as the plan view.

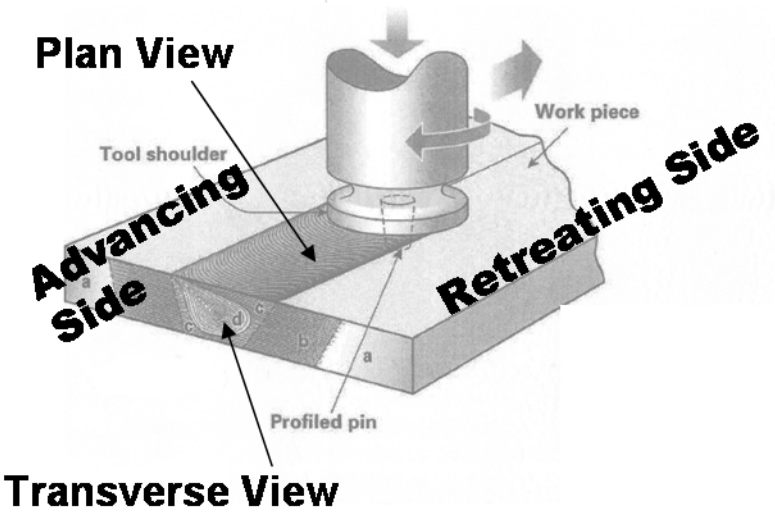

Figure 1 Conventional FSW Terminology

The cross-section (transverse view) of the resulting joint, shown in Figure 2, consists of three distinct metallographic regions; a nugget, a thermo-mechanically affected zone (TMAZ), and a heat affected zone (HAZ). In the TMAZ region, the parent material (PM) grains show evidence of mechanical deformation as they elongate from the HAZ toward the nugget region. The nugget region consists of refined grains.

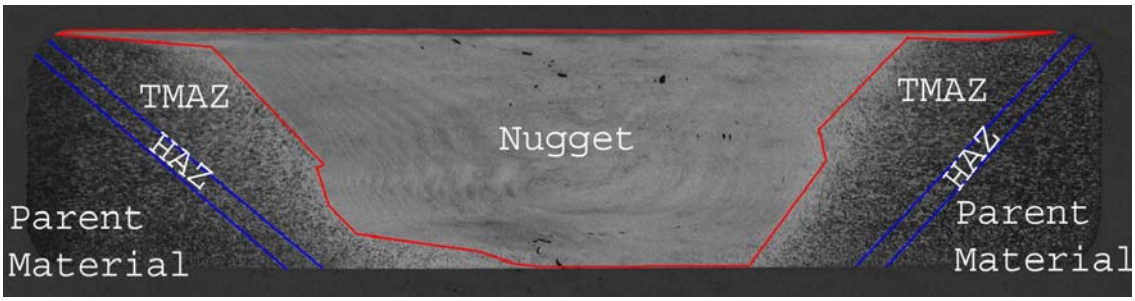

Figure 2 Transverse View of a Conventional FSW

The FSW tool consists of a shoulder and a pin. Figure 3 is an illustration of the conventional FSW setup for a simple butt weld. The work-pieces to be joined are butted together and clamped to an anvil. The pin of the FSW tool is plunged into the material along the seam formed by the work-pieces while the shoulder contacts the surface of the work-pieces. The rotating FSW tool traverses along the seam between the butted work-pieces to form the weld. The shoulder of the FSW tool, the PM and the backing anvil hydrostatically confine the softened weld material.

A typical FSW tool has a threaded pin, as shown in Figure 3, and either a scrolled or smooth shoulder. Figure 4 shows an FSW tool with a scrolled shoulder (a) and a smooth shoulder (b). When the shoulder of the work-piece is smooth, the process is usually performed with the FSW tool tilted at a slight lead angle as shown in Figure 3 [2]. A scrolled shoulder possesses features that aid in gripping the surface of the work-piece and is typically used with a zero degree tilt angle. Colegrove has reported that the shoulder of the FSW tool not only confines the material being stirred, but is also the major source of heating, by friction, in the FSW process [3]. The remainder of the heat input, up to 20% of the total, is reported to be generated by either friction between the pin and PM or deformational heating generated within the PM [3, 4].

Reported temperatures measured in the solid state FSW process are approximately $0.8T_{mp}$ [5, 6], however peak temperatures as low as $0.6T_{mp}$ have been reported [7]. A reported TEM study of the microstructure in a FSW is in agreement with the reported temperature values [8].

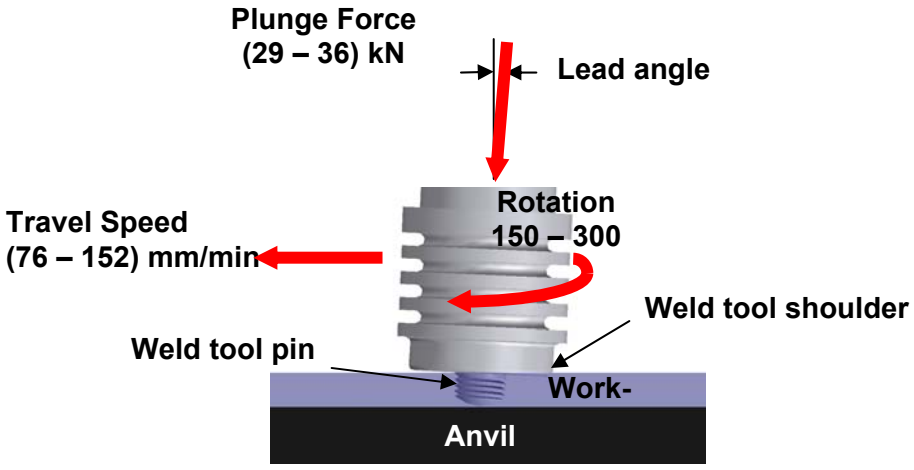

Figure 3 Schematic of the Conventional FSW Process [2]

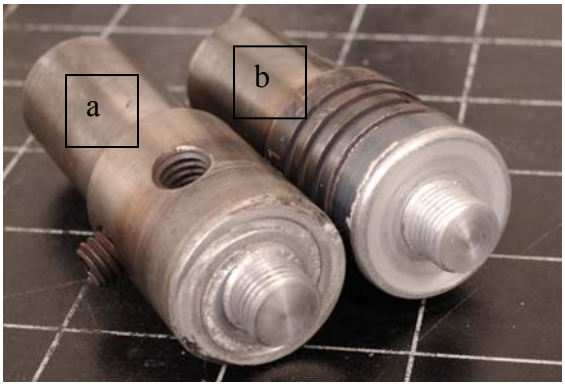

Figure 4 FSW tool with a scrolled shoulder (a) and a smooth shoulder (b)

The variable process parameters for FSWing are the tool travel speed, the tool plunge force and the tool rotation rate. Typical values for some key FSW parameters used on 2xxx series aluminum alloys, 0.25 to 0.5" thick, are summarized in Figure 3 [9]. Although the use of a weld seam location offset in FSWing is common practice at NASA, the offset is used to mitigate surface contaminants, and in the absence of contaminants does not have an effect on the weld strength [10]. This has been verified among the tensile specimens tested in this study and summarized in Appendix A.

CHAPTER II

BACKGROUND

Efforts to understand the physics of the metal flow during FSWing have included both theoretical and experimental studies. Various attempts to numerically model the physics of the FSW process are documented in the literature and include: thermal [11, 6, 12], thermo-mechanical [4], kinematic [13], and hydro codes [14]. Complimentary experimental studies have used various markers to trace out the material flow in FSWing [9, 2, 15, 16, 17, 18]. Additional studies have explored the use of computational fluid dynamics (CFD) which specifies a viscosity for the plasticized metal [3, 19, 20]. It should be noted that the CFD approach doesn't physically capture the behavior of a crystalline solid; therefore these studies are not summarized in this background review.

Theoretical Models

Various theoretical approaches have been used to study the physics of the FSW process. Typically these approaches use various mathematical relationships for the heat generation and resulting flow properties of the metal. These relationships are input into finite element analysis (FEA) to generate two and three dimensional data images of the thermal profile within the FSW. In general, two-dimensional models describe the thermal field perpendicular to the axis of tool rotation, or the plan view, while the three-

dimensional models additionally address the through material thickness thermal field [6, 11, 12, 4].

Initial thermal models treated the FSW tool as a moving heat source which generated a thermal profile. An initial analog model by McClure [6] used the Rosenthal equation in an attempt to predict the temperature profile around the FSW tool based on the thermal conductivity of the work-piece. Chao and Qi [11], using a common FEA code, assumed that friction between the FSW tool and work-piece was responsible for the heat generation. Heat was applied to the work-piece surface, simulating frictional heat developed by the tool shoulder. Frigaard [12] used the finite difference approach to model the thermal fields based on a variable frictional coefficient. This variable frictional coefficient governed the maximum temperature in the model to tune the temperature to match experimental results. Though a majority of the heat was assumed to be generated by the FSW tool shoulder, heat generated by the FSW tool pin was also included. This early model suggests that the contact conditions between the weld tool and the work-piece are not constant.

By controlling or varying the frictional coefficients, results of the various modeling approaches were found to be in close agreement with temperatures measured using instrumented panels during FSWing [6, 11, 12]. Both the models [6, 11, 12] and the experimental studies indicate that the peak temperature occurs in the work-piece material along the weld centerline and that the temperatures decrease through the thickness of the work-piece. These studies assumed a symmetrical flow field around the weld tool and didn't consider the asymmetric nature. Because of the asymmetrical nature

of the flow fields, other experimental studies have found discrepancies in whether the peak temperatures can occur on the RS or the AS of the FSW [5, 21]. It should be noted that reported experimental information about the temperature profile at the FSW tool and work-piece interface is limited due to the consumption of the thermocouples near the tool during FSWing.

Although a temperature profile could be estimated using these early numerical models, the interaction between the FSW tool and its effect on resulting material flow was not accurately modeled. To couple these effects, subsequent thermo-mechanical models were developed to incorporate the heating and its effect on the mechanical properties of the metal during the FSW process. This modeling approach has required assumptions to be made regarding the contact conditions between the FSW tool and the work-piece as well as levels of strain applied at a given strain rate. Incorporating the material flow stresses in conjunction with the thermal profile requires access to a material database to provide properties at the levels of strain and strain rate imposed on the metal by the FSW process. Accurate estimates of the hot forming conditions experienced by the metal during this process are necessary to guide material testing to generate these databases.

Colegrove expanded his earlier modeling efforts to mate a mechanical model to his thermal model [4]. This thermo-mechanical model considered the material flow around the FSW tool during welding and considered heat generation from both frictional and material shearing sources. Colegrove has also reported results from two dimensional and three dimensional models using CFD analysis techniques [3,19]. In the three

dimensional model, contact conditions were assumed to be full stick in which the material sticks to the FSW tool with no velocity discontinuity while the two dimensional model allowed for a slip condition between the work-piece and FSW tool. Colegrove [19] treated the numerical approach as steady-state. However, results from Colegrove's model [19] predicted a peak welding temperature 56% greater than those observed experimentally. There are two possible causes for this discrepancy. Colegrove's model could be predicting temperatures that were not captured in the experiments due to the consumption of the thermocouples near the FSW tool. The other possibility is that the model is predicting high peak temperatures due to the assumed, and not experimentally correlated, full stick condition between the work-piece and weld tool.

Nunes [13, 22, 23] has proposed a kinematic flow model that considers the metal flow as influenced by the processing parameters. This kinematic flow model consists of three incompressible flow fields shown in Figure 5. As the rotating FSW tool plunges into the work-piece, the interaction causes a seizing between the FSW tool and the work-piece, resulting in a rotating plug of metal (Figure 5a). This rotating plug of metal is then uniformly translated with the rotating FSW tool along the weld seam (Figure 5b). The threads on the FSW tool produce a "vortex" flow field (Figure 5c) that carries material downward near the tool pin, outward near the bottom of the work-piece, upward along the outside of the nugget region, and inward near the shoulder of the tool.

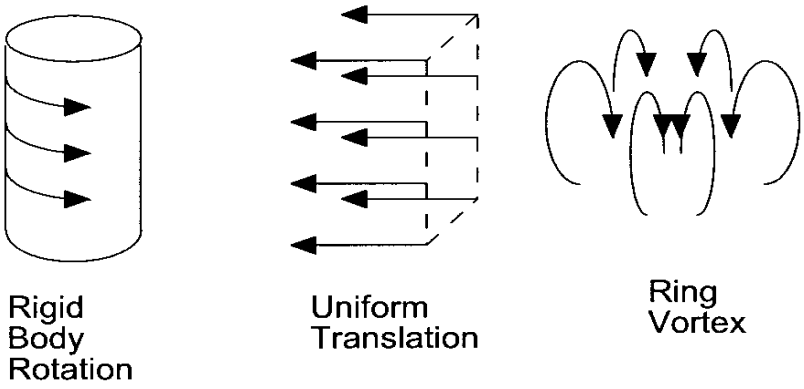

Figure 5 Nunes' Kinematic Model breaks the movement of metal flow into 3 incompressible flow fields. As the FSW tool seizes the metal, it provides a rigid body rotation (a) which is uniformly translated along the weld seam (b). Threaded features impart a ring vortex flow through the metal thickness (c). [23]

These three incompressible flow fields combine to predict metal flow along two possible paths, the straight-through current and the maelstrom current, during the FSW process. These paths are shown in Figure 6 [13, 23]. The straight-through current flow path predicts that metal will pass through the weld zone, being affected only by the translational flow field. Thus, the material on the RS of the FSW is predicted to follow the translational flow and is deposited behind the FSW tool without much lateral change in position. Material that enters further toward the AS, has a greater tendency to be retained in the rotating plug at the shoulder, where the ring vortex radial velocity component is inward, and to be prematurely ejected from the rotating plug further down the pin where the ring vortex radial velocity component is outward. This flow is the maelstrom current which results in a downward flow of fine grained nugget material with parent metal flow into the transverse section near the shoulder and a bulge of fine grained

metal further down the pin. The resulting structure is unsymmetrical because of the AS/RS entrance location effect.

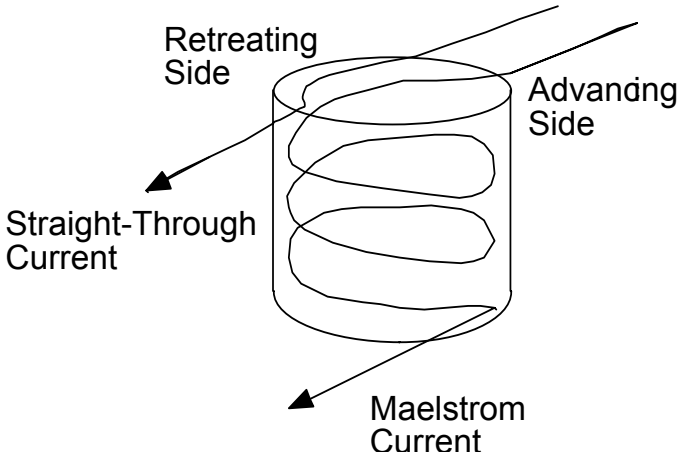

Figure 6 Combining the 3 incompressible flow fields from Figure 5, results in 2 inter-twined flow paths. [2]

Although the Nunes' Kinematic Model doesn't provide information on the heat profile or its effects on the surrounding metal, it does provide a basis for estimating the strain rate the metal is subjected to during the FSW process. Using the Nunes' Kinematic model, the strain ($\Delta\gamma$) and strain rate (γ_{dot}) can be calculated using equations 1 and 2, respectively.

$$\Delta\gamma = R\Omega/V \qquad \text{[eqn. 1]}$$

$$\gamma_{dot} = R\Omega/\delta \qquad \text{[eqn. 2]}$$

Where R is the shear surface radius, V is the weld travel speed, Ω is the tool rotational speed in radians/second, and δ is the thickness of the shear surface. Estimates of the shear surface thickness have been based on the metallographic image shown in Figure 7. Based on microstructural observation, this thickness is estimated to be on the

order of 0.01 times the tool diameter. The estimated strain ($\Delta\gamma$) and strain rate (γ_{dot}) are summarized for this study in Table 1 as a function of the process parameters used in this study which are also summarized in Figure 3 for the 12.7 mm diameter FSW pin (D_{pin}) used in this study.

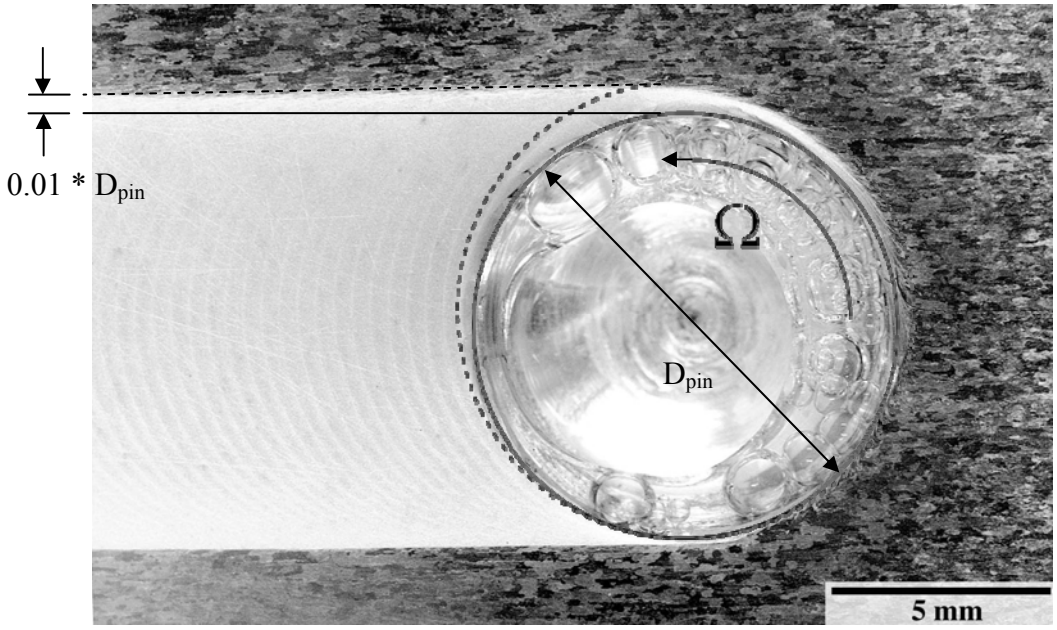

Figure 7 Estimation of shear surface thickness [Figure supplied courtesy of Dr. Arthur C. Nunes, Jr., NASA-MSFC]

Table 1

Maximum/Minimum Strain Rate per Process Parameters in Figure 3

Weld Travel Speed (mm/min)	Tool Rotational Speed (rev/minute)	Strain	Strain Rate (s^{-1})
76	300	315	1.2×10^3
152	150	158	2.4×10^3

A correlation between the metal working conditions of temperature, strain, and strain rate and the resulting microstructure has been lacking in previous models. Solid mechanics approaches using FEA analysis consider the problem as one of small strains (<2 - 5%) and low strain rates (<10 s^{-1}). Thus a different numeric approach is needed to model the large strains at high instantaneous strain rates predicted by the Nunes' Kinematic model.

More recent models have begun to consider hybrid codes, where aspects of various modeling approaches are used at appropriate stages of the weld process [24]. However, details of these approaches are considered to be beyond the scope of this research project.

Experimental

Various marker studies have been used to trace out the metal flow, including: embedded steel shot [15], aluminum alloy inserts [16,17], copper plating [18], tungsten wire [9], and lead wire [2]. Post weld inspection used X-ray radiography to document the resulting marker placement after the FSW. Initial studies [15] with 380 μm diameter steel shot showed the metal flow to follow orderly paths as influenced by the location of entrance into the weld zone and the processing parameters. Use of finer 25 μm diameter tungsten wire [9] allowed individual flow streams to be traced out in the weld zone with a higher resolution. Variations in the resulting wire marker post weld position were found to correspond with the Nunes' Kinematic Model [9]. Tungsten wire introduced into the FSW on the RS of the FSW tool correlated with the prediction of straight through flow

[9]. As the wire was introduced into the FSW on the AS of the FSW, the post weld path of tracers were found to have been affected by the theorized maelstrom flow [9].

Further wire tracer studies were conducted using 250 μm diameter lead wires [2]. At the temperatures predicted during FSWing of aluminum panels, the lead wire is expected to be molten and provide a continuous tracing of the metal flow during the FSW process. This study showed variations/oscillations in the post-weld patterns of the lead wire [2]. From this study, it was theorized that variations in the contact condition between the FSW tool and the work-piece could result in the variations observed with the lead wire tracer. The authors theorized a stick-slip condition occurring which seems in agreement with the results from the interface conditions assumed by Colegrove et al in their attempts to model the process using CFD analysis [2, 3, 19, 25, 26].

As a result of changing boundary conditions at the FSW tool/work-piece interface, the contact conditions may fluctuate between full sticking, causing shearing deformation in the PM, and varying degrees of slipping causing friction to be generated between the FSW tool and the work-piece. It has been proposed that this provides a method of regulating the temperature [2]. As the work-piece / FSW tool experiences sticking, the PM shears, resulting in heating contributions [7]. As the temperature increases, the consequent softening of the metal results in slippage between the work-piece and FSW tool. As the heating contributions decline, the work-piece cools off. At sufficient temperatures, the work-piece/FSW tool starts seizing again. It has been theorized that the previously mentioned stick-slip condition influences the amount of material that is swept during the FSW tool rotation [2]. The varying amounts of swept

material should result in a variance in cross-sectional nugget area and shape when observed from a transverse view. The influence of the stick-slip condition on the nugget area, which is distorted by ring vortex flow into the nugget area, is illustrated in Figure 8.

Both theoretical and experimental studies indicate the contact conditions between the work-piece and weld tool are unknown and may vary during the FSW process. To provide insight into the contact conditions, the objective of this study is to characterize the FSW nugget in terms of swept volume as indicated by the cross-sectional area and symmetry of the FSW nugget over a range of processing conditions. Physical characteristics and mechanical properties of the rotating volume of metal will be inspected to determine if the nugget displays variations that could be caused by variations in work-piece / FSW tool interactions. These variations will be correlated with mechanical property measurements to determine if the theorized stick-slip condition is beneficial or detrimental to the FSW properties.

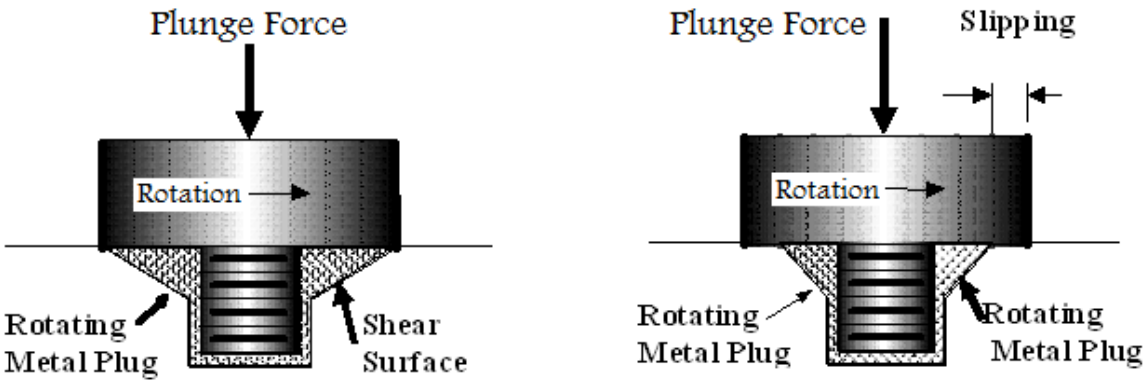

Figure 8 Effect of changing interface conditions on the swept volume represented by the rotating plug which forms the FSW nugget [2]

If the theorized oscillations in nugget volume occur, evidence should be observed in the cross-sectional area or symmetry of the FSW nugget. To document any variations in the symmetry or cross-sectional area of the FSW nugget, transverse images were analyzed. To correlate variations with mechanical properties, miniature tensile specimens were prepared from the corresponding FSW nuggets.

CHAPTER III

EXPERIMENTAL PROCEDURE

A series of FSW butt welds were made using rolled panels of aluminum alloy 2219-T87 approximately 610 mm long, 152 mm wide, and 6.35 mm thick. The FSWs used in this study were made at NASA's Marshall Space Flight Center in Huntsville, AL [27]. The FSW tool, shown in Figure 4a, consisted of a 12.7 mm diameter UNF left handed, threaded FSW tool with a scrolled shoulder 30.5 mm in diameter and a pin length approximately 6.2 to 6.3 mm. All FSWs were performed with a zero degree lead angle.

To establish nominal conditions for the AA2219 FSW panels, a number of bounding panels were FSWed at the NASA-MSFC to establish processing conditions producing adequate weld quality as evidenced by full scale tensile tests conducted perpendicular to the weld direction [27]. Off nominal conditions were then selected that were within the desired process parameter window. FSW parameters are summarized in Table 2 for the 2219 panels. The effect of varied plunge force was studied in Series A. "Hot" or "cold" FSW variations were studied in Series B and C. A "hot" weld is one with a higher RPM or slower travel speed. A "cold" weld is one with a lower RPM or higher travel speed.

A layout of the FSW panel is shown in Figure 9. Each nominally 610mm long FSW panel was subjected to either a systematic variation of travel speed, RPM, or plunge force while maintaining the other two parameters constant. A 25.4 mm transition region separated each parameter change, resulting in a 165 mm weld length to characterize each parameter. Characterization of each FSW was made using the last 50 mm segment as illustrated in Figure 9.

Table 2

Variation of FSW Processing Parameters

Series	Nominal Processing Parameters		
	Tool Travel speed (mm/min)	**Tool RPM**	**Tool Plunge Force (kN)**
A	114	200	29, 31, 36
B	114	150, 200, 300	31
C	76, 114, 153	200	31

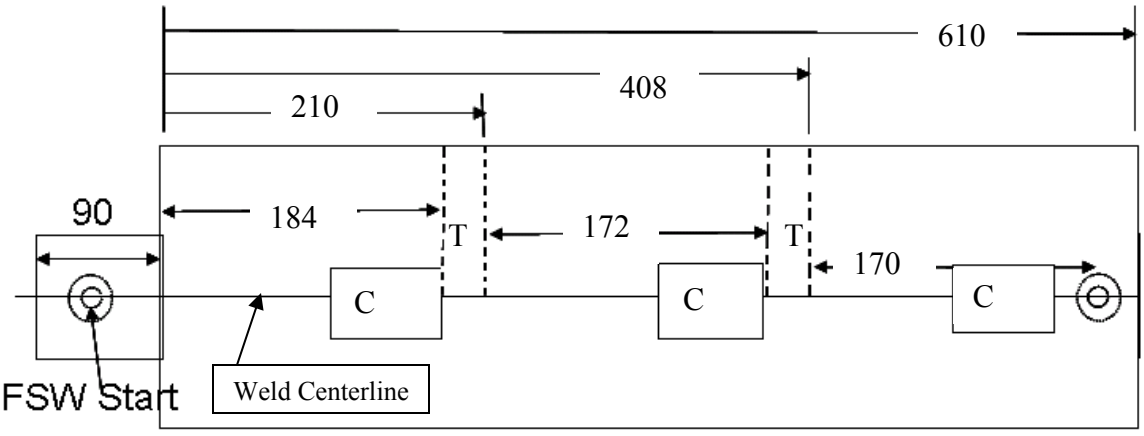

Figure 9 Schematic of FSW panel layout with "T" denoting transition region and "C" denoting material used for characterization. All dimensions are in mm.

Table 3 summarizes the FSW panels characterized in this study. There were five possible locations of the weld centerline (butting surfaces of the work-pieces) in relation to the centerline of the FSW tool. Figure 10 defines the centerline offset of the FSW tool and the butting surfaces of the work-pieces. As noted in Table 3, the specimens used for this study were taken from a total of 15 weld panels; 5 panels each for plunge force variation, tool RPM variation, and travel speed variation. As summarized in Table 3, each process parameter variation evaluated included specimens at varying weld centerline offsets.

Table 3

FSW Panel Identification

Sample ID	Centerline Offset (mm)	Variation
C01	6.096 RS	Load
C16, C18	6.096 RS	RPM
C31, C32, C33	6.096 RS	Travel
C05	3.048 RS	Load
C21	3.048 RS	RPM
C35, C36	3.048 RS	Travel
C07, C08, C09	0	Load
C22	0	RPM
C39	0	Travel
C12	3.048 AS	Load
C26, C27	3.048 AS	RPM
C41, C42	3.048 AS	Travel
C13, C14	6.096 AS	Load
C28, C30	6.096 AS	RPM
C44, C45	6.096 AS	Travel

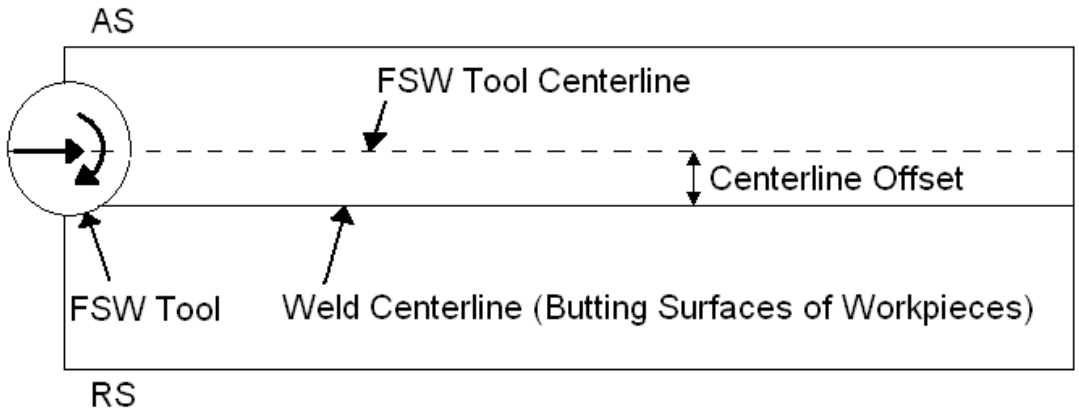

Figure 10 FSW centerline offset definition

Metallographic Procedure

Metallographic specimens were taken of the transverse section of each FSW segment as indicated in Figure 9. The samples were cut using a metallographic cut off saw from the end of each FSW segment to evaluate the steady-state characteristics. The specimens were mounted and polished using standard metallurgical procedures. All samples were etched using Keller's Reagent to document the macrostructure. Images were recorded using a Nikon D1 camera with zoom lens.

In an accompanying study at MSU [28], representative grain size measurements were made for 3 samples, at varying RPM, using electron backscattered diffraction / orientation image mapping. These samples are classified as series B FSWs as defined in Table 2. Table 4 indicates the variation in grain size observed between the AS and RS of the FSWs.

Table 4

Grain Size Measurements [28]

Specimen	Grain Size (μm)
C29-150 AS	2.5
C29-150 RS	1.8
C29-200 AS	2.8
C29-200 RS	2.6
C29-300 AS	4.1
C29-300 RS	4.2

Mechanical Property Testing Procedure

To evaluate the mechanical properties of only the nugget of the FSW, tensile specimens were designed with the gage section entirely within the transverse section of the FSW nugget as shown in Figure 11a. The geometry was first machined, and then sliced using wire EDM, into individual specimens as shown in Figure 11b and Figure 11c. The tensile specimens are 2.0 cm long x 0.64 cm wide x 0.03 cm thick. The recast layer on an EDM wire cut is approximately 0.0003 to 0.0005 cm thick. Considering the thickness of the specimen at 0.03 cm, the recast layer is approximately 1-2% of the material thickness. Using rule of mixtures for the resulting mechanical properties, this recast layer would be expected to affect the material properties by 0.8 to 1.6%. Thus the effect of the recast layer is assumed to be negligible.

For this study, a total of 48 FSWs were evaluated. Three tensile specimens were machined from each weld section. Specimens were tested in uni-axial tension using a stepper motor driven miniature tensile tester designed and fabricated at MSU [29].

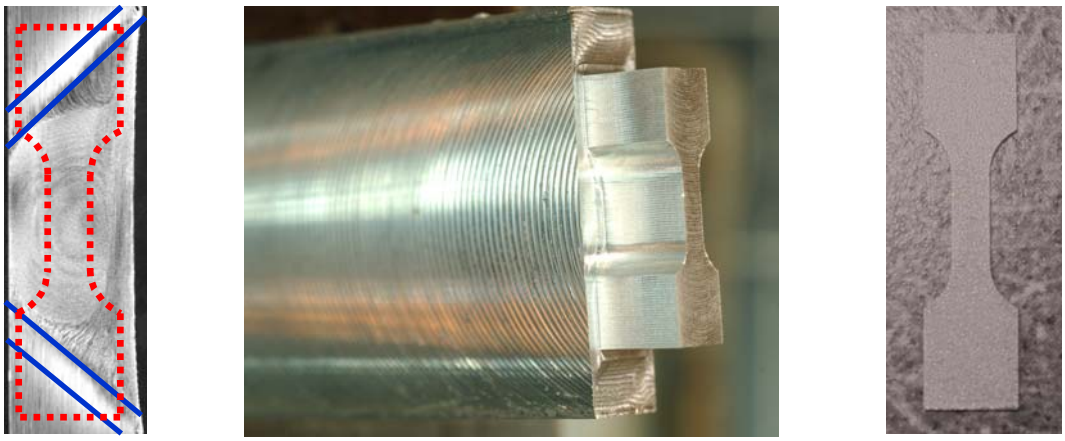

(a) (b) (c)

Figure 11 Miniature tensile specimens fabricated from the FSW nuggets. Shown are the specimens from the FSW transverse microstructure with the specimen geometry superimposed (a). An end mill was used to machine the dogbone geometry (b) which was then sliced into individual specimens (c) using wire EDM.

All tests were run at ambient temperature at a constant crosshead velocity of 0.05 mm/min. The data acquisition tool LabVIEW was used to acquire data at a rate of 1 sample per second. The data acquisition program used for this study was a modified version of Howard's [29]. Inputs for the program included extension rate, data capture rate, specimen width, specimen thickness, and specimen gage length. Time, displacement, and load values were recorded. The specimen cross sectional area (equation 3) was calculated and used to calculate the resulting specimen engineering stress (equation 4) and strain (equation 5) within the data acquisition program. All of the above parameters were output in tab-delimited format and converted to an Excel file for post processing. The variables listed in equations 3 through 5 are defined in Table 5.

$$A_{cross\text{-}section} = Width_{specimen} \times Thickness_{specimen} \quad \text{(eqn. 3)}$$

$$\sigma = F/A_{cross\text{-}section} \quad \text{(eqn. 4)}$$

$$\varepsilon = extension/L_{gage} \quad \text{(eqn. 5)}$$

Table 5

Equation 3-5 Variables

Variable	Description
σ	Engineering stress
ε	Engineering strain
$Width_{specimen}$	Initial width of the tensile specimen within the gage section
$Thickness_{specimen}$	Initial tensile specimen thickness within the gage section
F	Resulting load reacted against the tensile specimen
$A_{cross\text{-}section}$	Initial tensile specimen cross-sectional area of the gage section
L_{gage}	Initial length of the tensile specimen gage section
extension	Change in gage section length during tension test

CHAPTER IV

RESULTS AND DISCUSSION

In establishing the acceptable parameter range for the FSWs used in this study, bounding panels were FSWed at the NASA-MSFC. Tensile properties of these full-size specimens, shown in Figure 12 (20.3 cm long x 2.5 cm wide), are summarized in Table 6. As noted, there is not an appreciable difference in the UTS measured. This may be due to variations in strength in the HAZ which affects the overall strength. By isolating the tensile specimens in this study to the nugget area only, the effects of the processing parameters on the final strength of the nugget material can be assessed.

Figure 12 Photograph of full scale tensile specimen used to establish range of acceptable FSWing parameters

Table 6

Tensile Strength of Bounding Parameter FSWs

Tool Rotation (RPM)	Tool Travel (in/min)	UTS (ksi)
150	4.5	43.6~44.0
175	4.5	44.9~44.8
200	2.5	44.1~43.2
200	3	44.5~44.1
200	4	45.1~45.4
200	4.5	45.9~46.0
200	6	41.6~46.3
300	4.5	36.0~40.7

For this study, each weld panel was subjected to a systematic variation of plunge force, tool RPM, or travel speed. For each set of processing parameters on a given panel, one transverse macroscopic cross section was mounted and polished, and three tensile specimens were machined and tested. Image processing was used to quantify the nugget features in the metallographically prepared transverse sections of the FSW. The cross-sectional area and symmetry of the FSW nugget were measured using a method similar to Zettler, et al. [30]. The area of the nugget region was defined as the region showing a "noticeable" amount of grain size reduction. The symmetry of the nugget was calculated from two angles, α and β, as shown in Figure 13. The angles were measured from the point that the tool overlay contacted the TMAZ to the point where the nugget material became parallel with the top surface of the weld, near the shoulder of the tool.

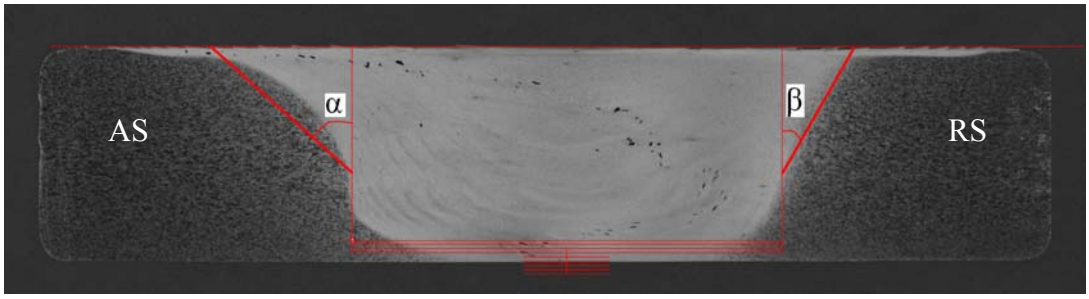

Figure 13 Characterization of the symmetry of the FSW nugget

The ratio of the angles α and β describe the FSW nugget symmetry. A ratio greater than one indicates a FSW nugget that is biased towards the AS of the weld while a ratio less than one indicates a FSW nugget that is biased towards the RS of the weld. The thickness of the PM plates ranged from 6.12 to 6.93 millimeters which produced a false scatter in the results of the measured nugget area. To reduce this false data scatter, an "effective width" was calculated based on the measured area of the nugget divided by an individual plate thickness. For this study the weld seam location is assumed to have no effect on the resulting FSW nugget geometry.

To consider possible trends between nugget characterization and mechanical properties a series of plots were made. Figure 14 summarizes the yield strength, effective width and the α/β ratio as the FSW tool RPM is varied. The yield strength and effective width versus tool RPM are shown in Figure 14a. While an approximate 25% increase is observed in yield strength as the FSW tool RPM increases, the effective width data scatter is reduced at higher RPM.

The yield strength and α/β ratio are plotted in Figure 14b versus FSW tool RPM. The average α/β ratio approaches symmetry with increasing RPM. However, increasing

scatter in the α/β ratio with increasing tool RPM indicates an increase in the variability of the nugget bias.

Figure 15 summarizes the yield strength, effective width, and α/β ratio as the FSW tool travel speed is varied. As the travel speed increases, the yield strength remains relatively constant. A slight decrease in the effective width and α/β ratio are observed as the travel speed increases. This suggests that increasing travel speed causes an oscillation in the FSW symmetry.

Figure 16 summarizes the yield strength, effective width, and α/β ratio as the plunge force is varied. Little variation is observed with nearly constant yield strength values and a slight increase in nugget effective width and non-symmetry towards the AS. The red horizontal lines on the following α/β ratio plots are a visual reference, indicating a symmetrical weld nugget.

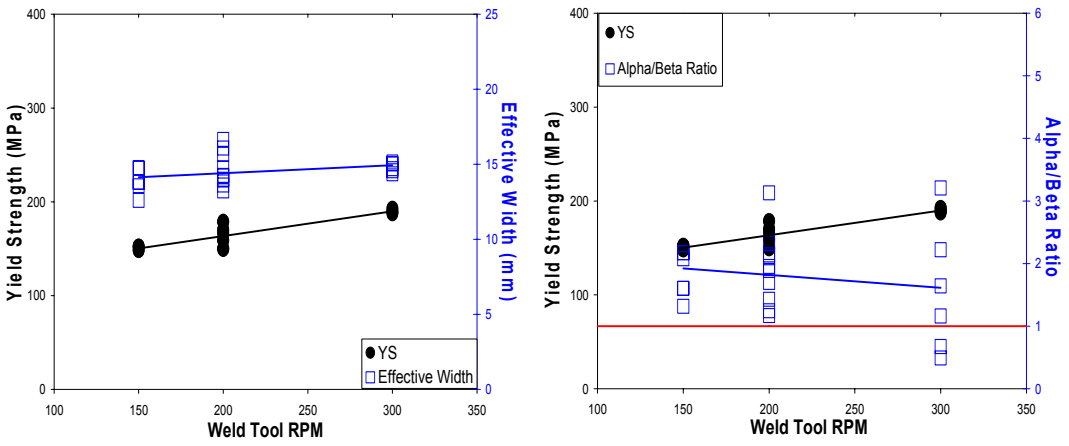

(a) (b)

Figure 14 Yield strength and (a) effective width and (b) α/β ratio versus FSW tool RPM

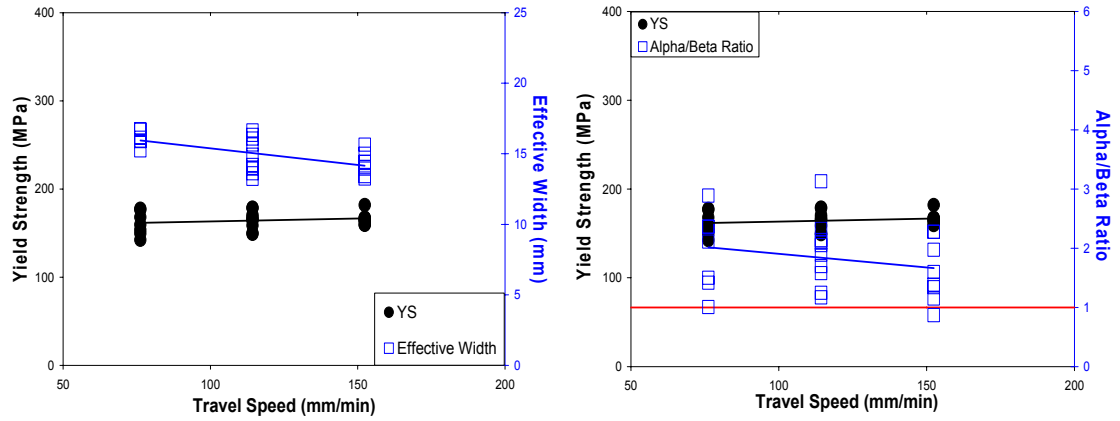

(a) (b)

Figure 15 Yield strength and (a) effective width and (b) α/β ratio versus travel speed

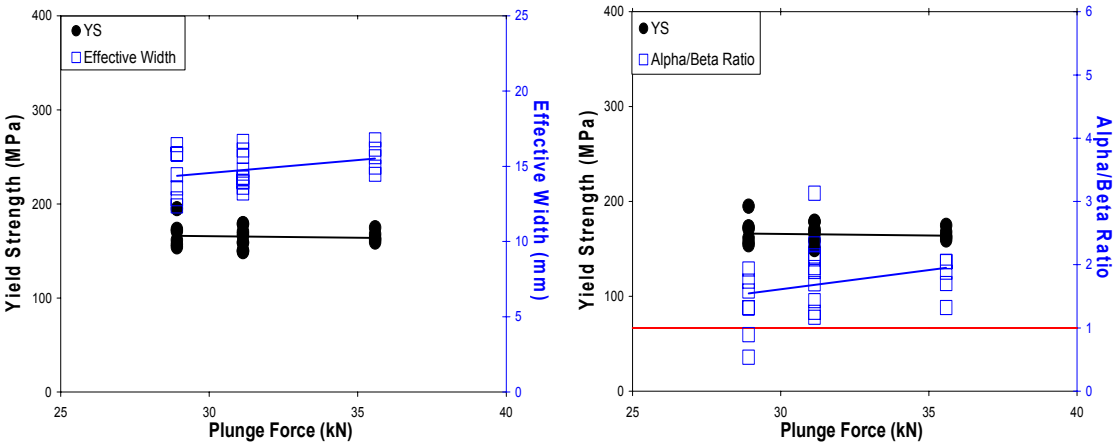

(a) (b)

Figure 16 Yield strength and (a) effective width and (b) α/β ratio versus plunge force

Plots of the UTS, effective width, and α/β ratio versus each of the three process parameters of interest are shown in Figures 17-19. Figure 17 summarizes the UTS, effective width, and α/β ratio as the FSW tool rpm is varied. As with the YS plots above, there is a noticeable increase in UTS with increasing FSW tool RPM. It is worthy to

point out that Figure 14 and Figure 17 show that an increase in nugget strength is accompanied by increasing FSW tool RPM and increasing scatter in the symmetry of the FSW nugget. Figure 18 and Figure 19 reflect the same basic trends in UTS as were seen in YS with varying FSW tool travel speed and plunge force.

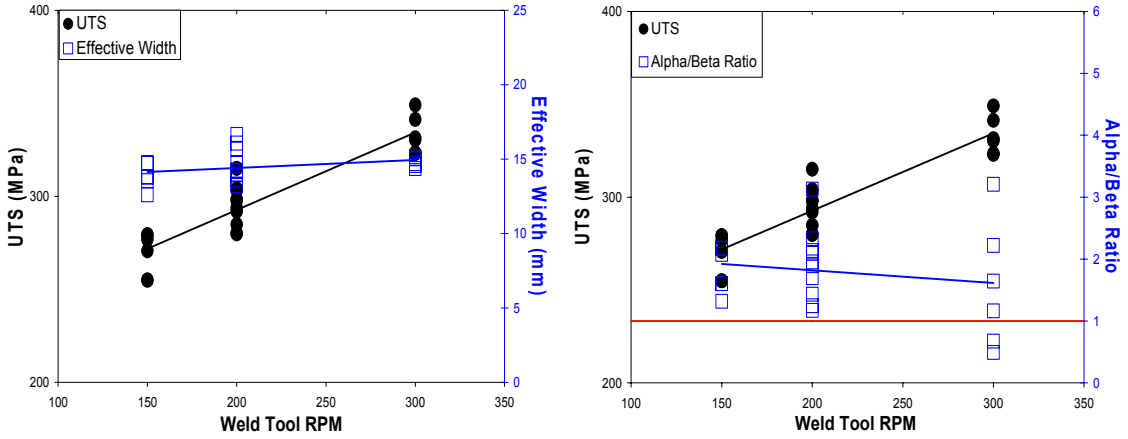

(a) (b)

Figure 17 Ultimate tensile strength and (a) effective width and (b) α/β ratio versus FSW tool rpm

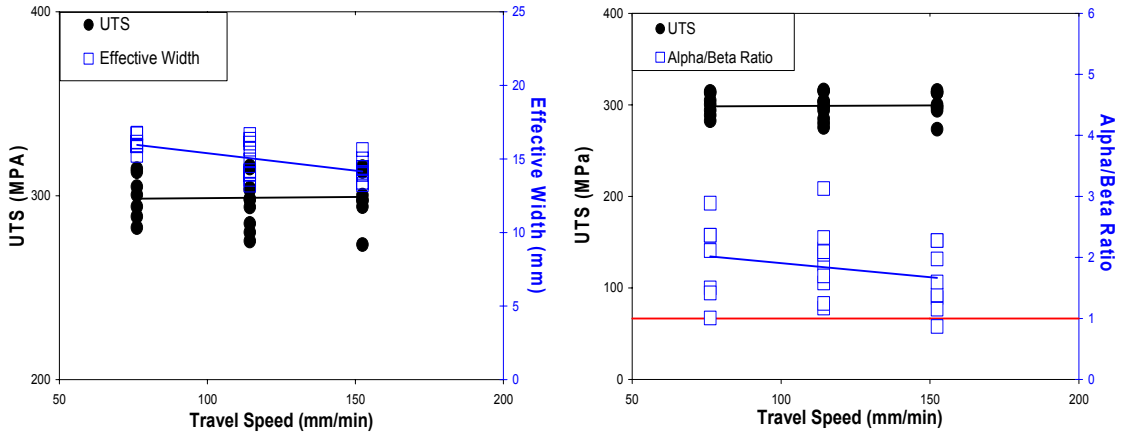

(a) (b)

Figure 18 Ultimate tensile strength and (a) effective width and (b) α/β ratio versus travel speed

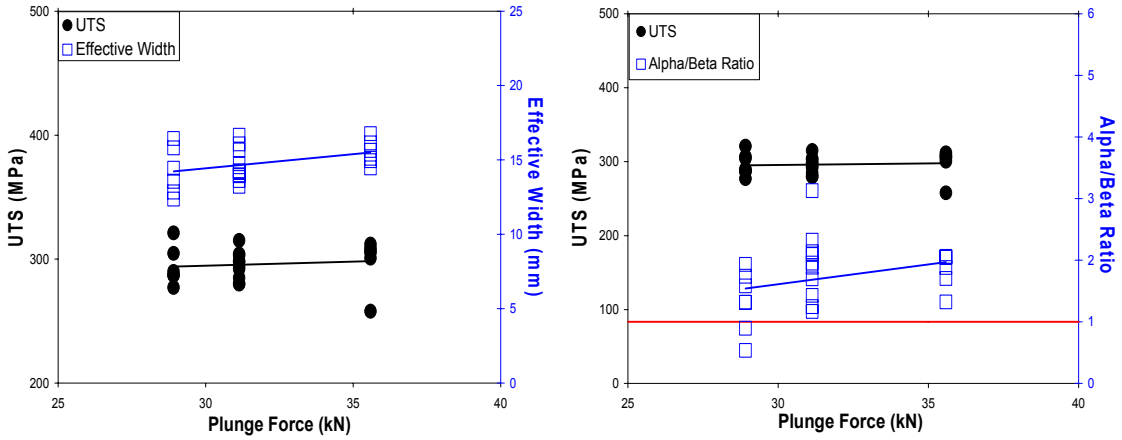

(a) (b)

Figure 19 Ultimate tensile strength and (a) effective width and (b) α/β ratio versus plunge force

The FSW tool RPM process parameter appeared to have the most effect on the strength of the weld nugget, with strength increasing at higher RPMs. The grain size measurements over the range of RPMs investigated showed a slight increase in the grain size as the RPM was increased. Although this seems at odds with grain size strengthening estimates obtained with the Hall-Petch relationship given in equation 6, an order of magnitude change would be required to effectively cause an increase in strength as summarized in Table 7 [31].

$$\sigma_{ys} = \sigma_o + k_1(d^{-0.5}) \qquad \text{[eqn. 6]}$$

Where:

σ_{ys} = yield strength

k_1 = material constant

d = average grain size

Table 7

Estimates of Increase in Yield Strength Due to Grain Size Strengthening [31]

d (μm)	σ_{ys}
100.0	39
80.0	44
60.0	51
4.0	197
2.0	278
0.1	1243
0.1	1758
0.0	3930

However, it is still expected that a grain size decrease from 4 to 2 microns should result in an increase in the σ_{ys}. Thus there must be some other factor influencing the final strength. Considering the significant amount of thermo-mechanical work the FSW nugget experiences, a variation in the dislocation density would also be expected along with the grain size variation. Equation 7 presents the relationship between dislocation density (ρ) and yield strength (σ_{ys}) where k_1 is a material constant [31]. Table 8 reflects the trend of increasing yield strength with increasing dislocation density.

$$\sigma_{ys} = \sigma_o + k_1(\rho^{-.5}) \qquad \text{[eqn.7]}$$

Table 8

Estimates of Increase in Yield Strength Due to Increased Dislocation Density [31]

Dislocation Density (cm/cm^3)	σ_{ys} (MPa)
$1x10^8$	37
$1x10^9$	118
$1x10^{10}$	374
$1x10^{11}$	1184
$1x10^{12}$	3744

A comparison of Table 7 and Table 8 indicates that the final yield strength in the weld nugget is a result of the effects of both grain size and dislocation density. Perhaps the final grain size observed is not due to the hotter temperature of the FSW as related to increased tool RPM, but rather a higher dislocation density indicative of more thermo-mechanical processing. However this is only a speculation and the use of transmission electron microscopy (TEM) would be required to obtain the dislocation density of the weld nugget.

Table 9 includes the standard deviation (σ_{dev}) and mean value of the α/β ratio versus FSW tool RPM and more clearly represents the scatter in the symmetry of the FSW nugget. Figure 14 and Figure 17, along with Table 9, indicates that the FSW tool RPM affects FSW nugget strength more than AS or RS bias of the weld nugget.

Table 9

Relationship Between α/β ratio and FSW Nugget Strength

FSW Tool RPM	Mean α/β Ratio	α/β Ratio σ_{dev}	Mean YS (MPa)	YS σ_{dev} (MPa)	Mean UTS (MPa)	UTS σ_{dev} (MPa)
150	1.8	0.3	151	2	269	11
200	1.9	0.5	163	11	295	11
300	1.6	0.9	190	2	333	9

There is no definite trend in the mean α/β ratio; however, there is a definite trend of increase in the standard deviation of the α/β ratio with increasing RPM. The mean values of YS and UTS also increase with RPM with no apparent accompanying trend in YS or UTS standard deviation.

CHAPTER V

SUMMARY AND CONCLUSIONS

For this study, three tensile specimens and one macrograph were prepared for each of the welds listed in Appendix B. The data indicates that the FSW tool RPM, within the parameters of this study, can result in an approximate 25% increase in the mechanical properties of the FSW nugget. Although there is scatter in the effective width of the nugget, this value remained relatively constant as the processing parameters were varied. If the torque required during FSWing is dependent on the amount of material moved, then this would suggest that a constant swept volume area corresponds to constant torque requirements during the FSW process.

When varying the FSW tool RPM and travel speed, variations were observed in the symmetry of the FSW nugget as indicated by a shift in the α/β ratio from a value greater than one toward a value of unity. This indicates that at the lower processing parameters (RPM and travel speed); a greater volume of swept material is present on the AS. As the processing parameters are increased, the symmetry is increased to represent a more balanced flow of metal between the AS and RS. The trend of increasing "scatter" of the α/β ratio with increasing tool RPM could be an indicator of changing contact conditions between the FSW tool and the work-piece [2]. The changing contact

condition could cause the oscillations predicted by the sticking and slipping of the FSW tool, theorized in previous studies [2, 26].

In this study, FSW tool RPM proved to have the greatest effect on the strength of the FSW nugget. This increase in strength cannot be attributed to grain size effects, but rather, differences in dislocation density. Since plastic deformation of a material results in increased dislocation density, the higher RPM was predicted to result in higher strain in the nugget region as summarized in Table 1.

Increasing FSW tool RPM resulted in increased weld nugget strength and an increase in the α/β ratio scatter. The test data supports that the theorized stick/slip condition [2, 26] is beneficial to the strength of the FSW nugget.

REFERENCES CITED

[1] W.M. Thomas et al., *Friction Stir Welding*, G.B. Patent Application No. 9125978.8; US Patent No. 5460317, Oct. 1995.

[2] J.A. Schneider, R. Beshears, A.C. Nunes, Jr. *Interfacial Sticking and Slipping in the Friction Stir Welding Process*, *Mat'l Sci. & Engr. A,*, 2006, vol. 435-436, pp. 297-304.

[3] P.A. Colegrove, H.R. Shercliff. *Two-dimensional CFD modeling of flow round profiled FSW tooling*, Science and Technology of Welding and Joining, Vol. 9, No. 6, pp. 483-492, 2004.

[4] P.Colegrove, M. Painter, D. Graham, T. Miller. *3 Dimensional Flow and Thermal Modeling of the Friction Stir Welding Process.* The 2nd International Symposium on Friction Stir Welding, Gothenburg, Sweden. June 2000.

[5] T.W. Nelson, R.J. Steel, W.J. Arbegast. *In situ thermal studies and post-weld mechanical properties of friction stir welds in age hardenable aluminum alloys.* Science and Technology of Welding and Joining. Vol. 8, No. 4, pp. 283-288, 2003.

[6] J.C. McClure, W. Tang, L.E. Murr, X. Guo. *A Thermal Model of Friction Stir Welding*. Proceedings of the 5th International Conference on Trends in Welding Research, Pine Mountain, GA, June 1998.

[7] S. Benavides, Y. Li, L.E. Murr, D. Brown, J.C. McClure. *Low-Temperature Friction-Stir Welding of 2024 Aluminum*, Scripta Materialia, Vol. 41, No. 8, pp 809-815, 1999.

[8] J.A. Schneider, A.C. Nunes Jr., P.S. Chen, G. Steele. *TEM Study of the FSW nugget in AA2195-T81*, Journal of Materials Science, Vol. 40, pp. 4341-4345, 2005.

[9] J. Sanders, *Understanding the Material Flow Path of the Friction Stir Weld Process*, MSME Thesis, Mississippi State University, 2005.

[10] Personal discussion with Dr. Judith Schneider, December 2009.

[11] Y.J. Chao, X. Qi, W. Tang. *Heat Transfer in Friction Stir Welding – Experimental and Numerical Studies*, Transactions of the ASME, Vol. 125, pp. 138-145. Feb. 2003.

[12] O. Frigaard, O. Grong, O.T. Midling. *A Process Model for Friction Stir Welding of Age Hardening Aluminum Alloys,* Metallurgical and Materials Transactions A, Vol. 32A, pp 1189-1200, May 2001.

[13] A.C. Nunes, Internal memo. NASA MSFC, 2005.

[14] A. Askari, S. Silling, B. London, M. Mahoney. *Modeling and Analysis of Friction Stir Welding Processes.* Proceedings of Symposium sponsored by the Shaping and Forming Committee of the MPMD of TMS. Nov. 4-8, 2001, Indianapolis, USA.

[15] K. Colligan, *Material Flow Behavior during Friction Stir Welding of Aluminum*, Supplement to the Welding Journal, pp. 229-237, July 1999.

[16] A.P. Reynolds, *Visualization of material flow in autogenous friction stirwelds*, Science and Technology of Welding and Joining, Vol. 5, No. 2, pp. 120-124, 2000.

[17] T. U. Seidel, A. P, Reynolds, *Visualization of the Material Flow in AA2195 Friction-Stir Welds Using a Marker Insert Technique*, Metallurgical and Materials Transactions A, Volume 32A, pp 2879-2884, 2001.

[18] Schneider, J.A., unpublished data, 2008.

[19] P.A. Colegrove, H.R. Shercliff. *3-Dimensional CFD modeling of flow round a threaded friction stir welding tool profile*, Journal of Materials Processing Technology, Vol 169, pp. 320-327, 2005.

[20] T.U. Seidel, A.P. Reynolds. *Two-dimensional friction stir welding process model based on fluid mechanics*. Science and Technology of Welding and Joining, Vol. 8, No. 3, pp. 175-183, 2003.

[21] M. Maeda, H. Liu, H. Fujii, T. Shibayanagi. *Temperature Field in the Vicinity of FSW-tool During FSWing of Aluminum Alloys.* Welding in the World. Vol. 49, No. ¾. 2005.

[22] A. C. Nunes, Jr., *Wiping Metal Transfer in Friction Stir Welding*, Aluminum 2001-Proceedings of the TMS 2001 Aluminum Automotive and Joining Sessions, Ed. S.K. Das, J.G. Kaufman, T.J. Lienert, pp. 235-248.

[23] Schneider, J.A., Nunes, Jr., A.C., "Characterization of plastic flow and resulting micro textures in a friction stir weld," *Met. Trans. B*, V. 35, p. 777-783, 2004.

[24] H. Schmidt, J. Hattel. *A Local Model for the Thermomechanical Conditions in Friction Stir Welding*, Modelling and Simulation in Materials Science and Engineering, Vol 13, pp. 77-93, 2005.

[25] P.A. Colegrove, H.R. Shercliff, *CFD modeling of friction stir welding of thick plate 7449 aluminum alloy*, Science and Technology of Welding and Joining, Vol. 11, No. 4, pp. 429-441, 2006.

[26] H. Schmidt, J. Hattel, J. Wert. *An analytical model for the heat generation in friction stir welding*, Modelling and Simulation in Materials Science and Engineering, Vol. 12, pp. 143-157, 2004.

[27] Schneider, J.A., "Toward understanding the material flow path variations in friction stir weld (FSW) processes," Final Report, NASA-MSFC Cooperative Agreement # NNM04AA14A, February 2006.

[28] J.A. Querin, A.M. Davis, J.A. Schneider. *Effect of Processing Parameters on Microstructure of the FSW Nugget.*

[29] A.M. Howard, "Design, Fabrication, and Verification of a Miniature Load Frame", MSME Thesis, Mississippi State University, May 2007.

[30] R. Zettler, et al., A Study on Material Flow in FSW of AA 2024-T351 and AA 6056-T4 Alloys, 5th Intl FSW Symp., 2004 France.

[31] J.A. Schneider, Thermal-Mechanical Processing in Friction Stir Welds, NASA summer faculty fellowship report, 2002.

APPENDIX A

UTS VERSUS WELD SEAM LOCATION

The plot below shows the value of UTS versus weld seam location for the RPM variation series of welds. Weld seam location is indicated on the horizontal axis of the plot, in millimeters, where the weld seam location is moved to either the AS or RS relative to the pin centerline (reference Table 3).

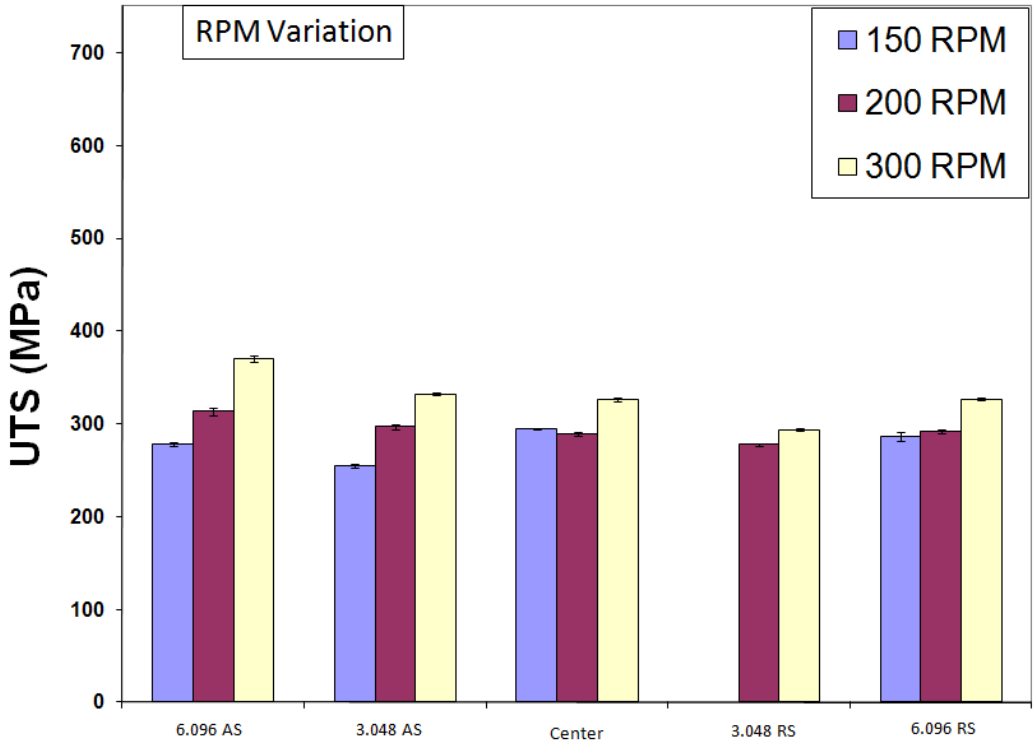

The plot below shows the value of UTS versus weld seam location for the travel speed variation series of welds. Weld seam location is indicated on the horizontal axis of the plot, in millimeters, where the weld seam location is moved to either the AS or RS relative to the pin centerline (reference Table 3).

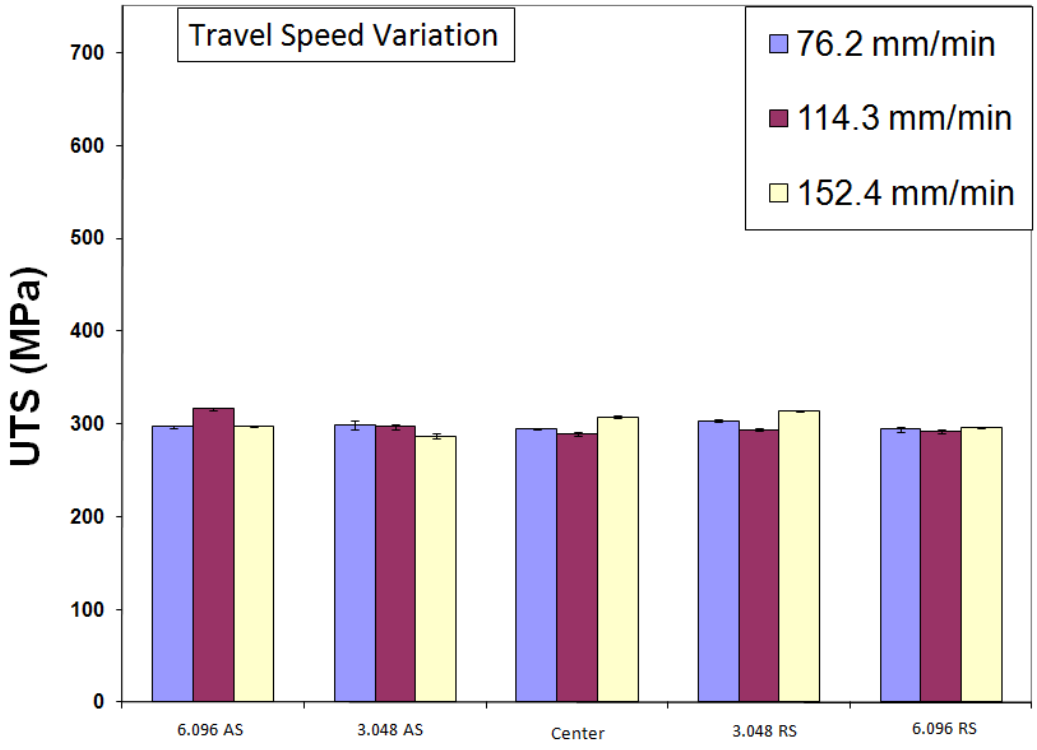

The plot below shows the value of UTS versus weld seam location for the plunge variation series of welds. There is no trend in UTS with respect to weld seam location. Weld seam location is indicated on the horizontal axis of the plot, in millimeters, where the weld seam location is moved to either the AS or RS relative to the pin centerline (reference Table 3).

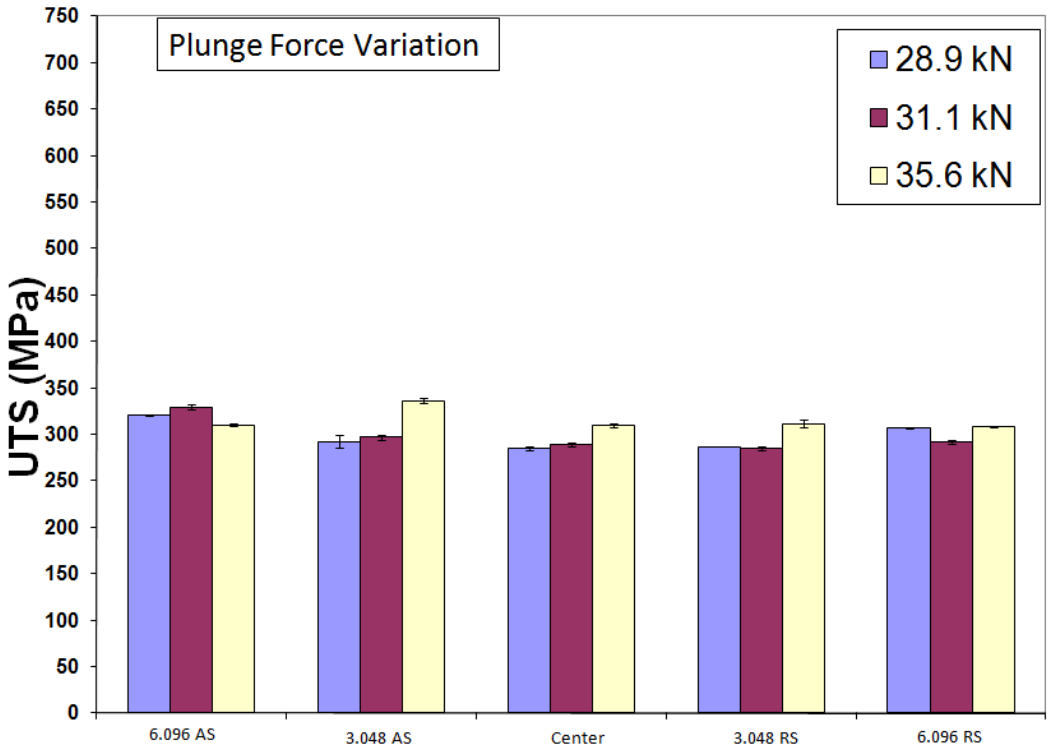

APPENDIX B

WELD NUGGET TENSILE DATA AND OPTICAL CHARACTERIZATION VALUES

Weld	YS (MPa)	UTS (Mpa)	Effective Width (mm)	Alpha/beta ratio	Plunge Force (kN)	RPM	Feed Rate (mm/min)
C01A - 6500	157.1	287.0	15.8	1.3	28.9	200	114.3
C01A - 7000	168.5	303.2	16.7	1.9	31.1	200	114.3
C01 - 8000	159.5	306.6	15.6	1.9	35.6	200	114.3
C01A - 8000	174.8	308.8	16.8	2.1	35.6	200	114.3
C05 - 6500	154.3	287.0	12.4	0.9	28.9	200	114.3
C07 - 6500	161.7	277.2	12.8	0.5	28.9	200	114.3
C07 - 7000	149.1	280.1	13.2	2.1	31.1	200	114.3
C07 - 8000	162.2	300.8	14.5	2.0	35.6	200	114.3
C08 - 6500	173.1	290.0	14.4	1.6	28.9	200	114.3
C08 - 7000C	179.2	297.9	13.9	1.2	31.1	200	114.3
C08 - 8000	167.8	312.1	14.9	1.3	35.6	200	114.3
C09 - 7000	164.1	275.4	14.9	1.6	31.1	200	114.3
C12 - 7000	150.4	292.0	14.3	2.0	31.1	200	114.3
C13 - 6500	195.0	304.6	13.6	1.9	28.9	200	114.3
C13 - 8000	154.8	258.0	15.1	2.1	35.6	200	114.3
C14 - 6500	171.1	321.1	16.4	1.7	28.9	200	114.3
C14 - 7000	166.2	316.1	16.3	2.1	31.1	200	114.3
C14 - 8000	163.5	305.2	16.1	1.7	35.6	200	114.3
C16 - 300	192.4	323.0	14.4	1.2	31.1	300	114.3
C18 - 300	189.3	330.4	14.7	0.7	31.1	300	114.3
C21 - 150	152.1	276.9	13.6	1.3	31.1	150	114.3
C22 - 300	187.2	331.4	15.0	0.5	31.1	300	114.3
C24 - 200C	158.7	304.1	14.2	2.3	31.1	200	114.3
C26 - 150	148.1	255.0	13.8	2.2	31.1	150	114.3
C26 - 200	150.2	284.9	13.6	3.1	31.1	200	114.3
C26 - 300	193.2	341.3	14.6	3.2	31.1	300	114.3
C27 - 300	189.5	323.4	15.0	1.6	31.1	300	114.3
C28 - 150	150.8	270.7	12.6	2.1	31.1	150	114.3
C30 - 150	152.8	279.3	14.7	1.6	31.1	150	114.3
C30 - 300	188.6	349.1	15.2	2.2	31.1	300	114.3
C31 - 6	160.1	297.9	14.0	0.9	31.1	200	152.4
C32 - 6	167.3	294.1	15.6	1.4	31.1	200	152.4
C33 - 4	159.1	279.9	14.7	1.4	31.1	200	114.3
C35-3	176.6	313.1	16.1	2.4	31.1	200	76.2
C35 - 4C	165.8	293.9	15.7	2.1	31.1	200	114.3
C35 - 6	164.2	313.2	14.4	2.3	31.1	200	152.4
C36 - 3	168.1	300.5	15.9	2.1	31.1	200	76.2
C39 - 3	153.8	294.1	15.9	1.0	31.1	200	76.2
C39 - 4	170.8	298.3	14.0	1.2	31.1	200	114.3
C39 - 6C	182.0	315.8	15.0	1.2	31.1	200	152.4
C41 - 3	177.8	314.7	16.7	2.4	31.1	200	76.2
C41 - 4C	178.3	315.0	16.1	1.7	31.1	200	114.3
C41 - 6C	167.6	273.5	13.4	2.0	31.1	200	152.4
C42 - 3C	142.4	282.7	15.9	1.4	31.1	200	76.2
C42 - 6	165.1	300.3	13.2	1.3	31.1	200	152.4
C44 - 3	149.7	288.7	15.2	1.5	31.1	200	76.2
C44 - 6	159.3	297.2	13.9	1.6	31.1	200	152.4
C45 - 3	159.7	304.9	16.7	2.9	31.1	200	76.2